Influence of laser–target interaction regime on composition and properties of surface layers grown by laser treatment of Ti plates

2009 J. Phys. D: Appl. Phys. 42 245303

(http://iopscience.iop.org/0022-3727/42/24/245303)

IOP PUBLISHING JOURNAL OF PHYSICS D: APPLIED PHYSICS

J. Phys. D: Appl. Phys. **42** (2009) 245303 (8pp) doi:10.1088/0022-3727/42/24/245303

Influence of laser–target interaction regime on composition and properties of surface layers grown by laser treatment of Ti plates

L Lavisse[1,5], P Berger[2,3], M Cirisan[1], J M Jouvard[1], S Bourgeois[4] and M C Marco de Lucas[4]

[1] Laboratoire Interdisciplinaire Carnot de Bourgogne, UMR 5209 CNRS-Université de Bourgogne, 1 allée des Granges Forestier, F-71100 Chalon-sur-Saône, France
[2] CEA/DSM/IRAMIS/SIS2M , CEA - SACLAY, F-91191 Gif sur Yvette, France
[3] CNRS - Laboratoire Pierre Süe, UMR CEA-CNRS 9956, CEA - SACLAY, F-91191 Gif sur Yvette, France
[4] Laboratoire Interdisciplinaire Carnot de Bourgogne, UMR 5209 CNRS-Université de Bourgogne, 9 Av. A. Savary, BP 47 870, F-21078 Dijon Cedex, France

E-mail: Luc.Lavisse@u-bourgogne.fr

Received 26 September 2009, in final form 24 October 2009
Published 30 November 2009
Online at stacks.iop.org/JPhysD/42/245303

Abstract

Surface laser treatment of commercially pure titanium plates was performed in air using two different Nd : YAG sources delivering pulses of 5 and 35 ns. The laser fluence conditions were set to obtain with each source either yellow or blue surface layers. Nuclear reaction analysis (NRA) was used to quantify the amount of light elements in the formed layers. Titanium oxinitrides, containing different amounts of oxygen and nitrogen, were mainly found, except in the case of long pulses and high laser fluence, which led to the growth of titanium dioxide. The structure of the layers was studied by x-ray diffraction and Raman spectroscopy. In addition, reflectance spectra showed the transition from a metal-like behaviour to an insulating TiO_2-like behaviour as a function of the treatment conditions.

Modelling of the laser–target interaction on the basis of the Semak model was performed to understand the different compositions and properties of the layers. Numerical calculations showed that vaporization dominates in the case of short pulses, whereas a liquid-ablation regime is achieved in the case of 35 ns long pulses.

(Some figures in this article are in colour only in the electronic version)

1. Introduction

Laser treatments are powerful tools for improving the mechanical properties and the chemical behaviour of metals and alloys. Laser can also modify metal appearance by the growth of a coloured surface layer. The composition and microstructure of the formed surface layers, usually including nanocrystalline and metastable phases, depend on the irradiation conditions and on the thermal properties of the target which determine the laser–target interaction regime.

In this field, many studies have focused on titanium and alloys because of their numerous applications in aeronautical, marine and chemical industries [1, 2]. Laser irradiation in air allows us to obtain surface layers containing different oxides and even nitrides in spite of their lower thermodynamic stability [1, 3]. Thanks to the good tribological properties of titanium oxides and nitrides, surface laser treatments can be used to overcome the issues related to the poor tribological

[5] Author to whom any correspondence should be addressed.

Table 1. Laser treatment conditions and properties of the different layers analysed in this work. τ is the pulse duration, n_p the number of impacts per point, F_{lp} the fluence per pulse, F_l the cumulated fluence and I the laser irradiance. S_Y and S_B layers were obtained with short pulses, L_Y and L_B layers were obtained with long pulses. S_Y and L_Y layers are yellow, S_B and L_B layers are blue.

Samples	S_Y	L_Y	S_B	L_B
τ (ns)	5	35	5	35
n_p	28		68	
F_{lp} (10^4 J m^{-2})	4.2		7.7	
F_l (10^4 J m^{-2})	118		524	
I (10^{12} W m^{-2})	8	1	15	2

Table 2. Physico-chemical properties of the four samples: thickness (e), roughness (R_a) and colorimetric properties represented by CIELab coordinates L^*, a^*, b^* and c^*.

Samples	S_Y	L_Y	S_B	L_B
e (μm)	3	5	3	30
R_a (μm)	0.8	2.1	1.6	6.4
Colour	yellow		blue	
L^*	59	59	41	54
a^*	6	5	1	−4
b^*	25	21	−2	7
c^*	25	22	3	8

properties of titanium [4, 5], such as highly unstable friction coefficients and low wear rate [6, 7]. In addition, surface layers grown by laser irradiation present a wide variety of colours that make them very attractive in jewellery and decorative applications [8, 9].

In previous papers [10–12], we reported the growth of coloured surface layers by pulsed laser irradiation of commercially pure titanium plates in air with a Nd : YAG Q-switched laser. Colours, going from yellow to purple, blue or green were obtained as a function of the imposed laser fluence.

Here, we investigate the influence of the laser pulse duration on the laser–target interaction regime for understanding the composition, structure and optical properties of yellow and blue surface layers grown using low and high laser fluences about 120 J cm^{-2} and 500 J cm^{-2}, respectively. With this aim, two lasers delivering pulses of 5 or 35 ns were used. The composition and distribution of light chemical elements in the surface layers were studied by nuclear reaction analysis (NRA), while x-ray diffraction and Raman spectroscopy were used for structural study, and reflectance measurements for optical characterization of the layers. Laser–target interaction was modelled on the basis of the Semak model [13] to understand the influence of the interaction regime on the properties of the layers.

2. Experimental

2.1. Laser treatments

Commercially pure (CP) titanium (grade 4) plates were used for surface laser treatments in air. Prior to laser exposure, the samples were mechanically polished before an electrolytic polishing to reach a very low roughness of reference surfaces ($R_a < 0.4\,\mu$m). The laser treatment process was described in a previous paper [11]. Basically, the focused laser spot was moved with a galvanometric system over the titanium substrate surface with a constant velocity to form parallel straight lines.

In this work, two Q-switched Nd : YAG lasers operating at 1.064 μm were used. The first laser source (Quantel Brilliant B model) delivers short pulses of 5 ns, while the second (Cheval Laser) gives longer pulses of 35 ns. Both laser spots were almost circular with a Gaussian energy distribution.

Table 1 summarizes the different treatment conditions set by varying both the number of cumulated impacts, n_p, and the laser fluence per pulse, F_{lp} (in J m^{-2}). The corresponding values of cumulated laser fluence $F_l = F_{lp} \cdot n_p$ (in J m^{-2}) and irradiance I (in W cm^{-2}) are also given in table 1. The aim was to obtain yellow (S_Y, L_Y) and blue (S_B, L_B) surface layers with both laser sources. S_Y and S_B layers were obtained with short pulses, whereas L_Y and L_B layers were obtained with long pulses. Indeed, yellow layers were obtained in the case of low cumulated fluence (118×10^4 J m^{-2}), while blue layers were grown with high laser fluence (524×10^4 J m^{-2}). Note that Nd : YAG–laser radiation can induce the ignition of a plasma plume in front of Ti targets for irradiance values of some 10^{12} W m^{-2} [14].

The thickness of the surface layers (table 2) was determined by optical or electron microscopy observations. It is worth noting the high thickness of the layer L_B, around 30 μm, while around 3–5 μm for the others (S_Y, L_Y and S_B).

A Veeco NT9100 optical profiler with vertical and horizontal resolutions equal, respectively, to 3 nm and 1 μm was used for roughness measurements in the vertical shafting interference (VSI) mode. The roughness of the layers is reported in table 2. It is worth noting that the roughness is sensitive to pulse duration: layers obtained with short pulse duration (noted S) have smaller roughnesses than the layers obtained with a longer one (L). Moreover, with constant pulse duration, an increase in the laser fluence induces an increase in the roughness. This fact is consistent with our previous findings [15].

2.2. Elemental analysis

To investigate the composition and distribution of light chemical elements in the layers, NRA was chosen as a powerful method for quantitative analysis of light elements such as carbon, nitrogen and oxygen without any influence of the chemical environment and a low influence of the roughness [16].

A 2 μm × 2 μm rastered deuteron microbeam, delivered by a 3.75 MV Van de Graff accelerator [17], was used to map and depth profile concentrations of oxygen and nitrogen up to 1 μm under the surface. Two beam conditions were chosen, either 920 keV, an optimum for oxygen quantification from ^{16}O(d,p$_1$)^{17}O nuclear reaction [18], or 1900 keV, less favourable for oxygen but with an enhancement of nitrogen signals [19], especially ^{14}N(d,α_1)^{12}C nuclear reaction. Backscattered deuterons and emitted protons and alpha particles were detected at an average angle of 170°

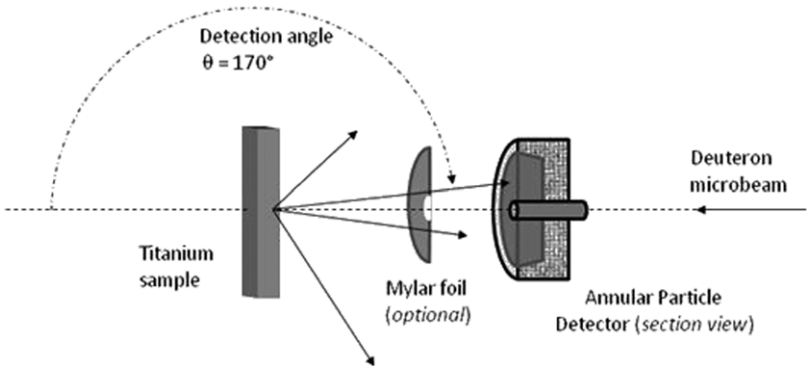

Figure 1. Sketch of NRA setup with a disc shaped particle detector. A central hole enables passage of the deuteron microbeam. According to beam conditions, a Mylar® foil may be placed before the detector to stop backscattered deuterons.

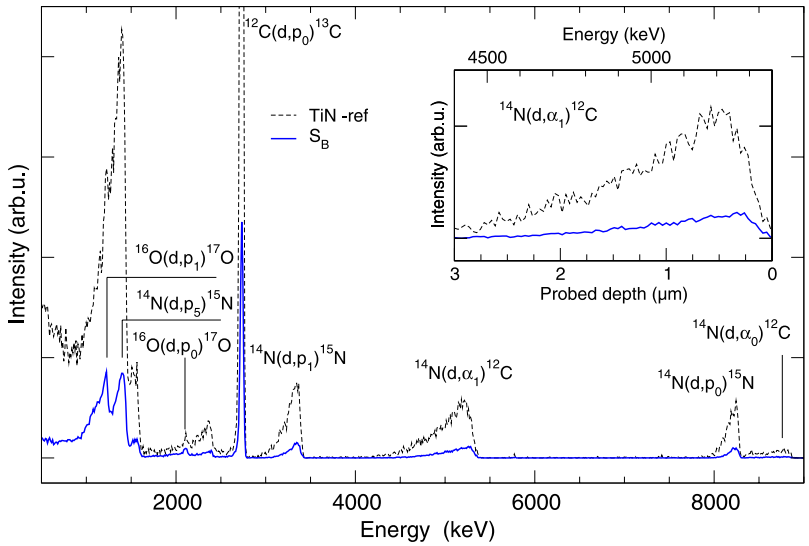

Figure 2. Global NRA spectrum obtained in experimental conditions optimized for nitrogen quantification (deuteron beam at 1900 keV, 12 μm thick Mylar foil): (dashed line) a nitrogen rich reference sample, so-called TiN-ref, and (solid line) sample S_B. Peaks corresponding to the different nuclear reactions are indicated.

by means of an annular surface barrier detector (figure 1). A central hole in the detector gives way to the microbeam. This configuration enables both a large solid angle (130 msr) and well-defined detection geometry. For layers containing a large amount of oxygen measured at 920 keV, the detector was covered with a 23 μm thick Mylar foil to stop backscattered deuterons and thus to have access to the whole oxygen depth profile without interferences. At 1900 keV, the detector remained uncovered to benefit from better depth resolutions for nitrogen profiles.

The concentration of oxygen and nitrogen is deduced from the energy spectrum of the emitted protons and alpha particles. Absolute quantification of these analyses involves normalization to the number of incident deuterons. Note that the same element may produce more than one peak when several nuclear energy levels are involved as shown in figure 2.

2.3. Physico-chemical characterization

Optical reflectance spectra were recorded at room temperature with a Konica-Minolta CM 3500d double beam spectrophotometer equipped with a 150 mm integrating sphere for diffuse reflectance measurements in the visible range in $d/8^\circ$ geometry. Colour specification of the films was represented in the CIELab colour space.

X-ray diffraction experiments were performed at grazing incidence with fixed incident angles in the 0.5°–8° range using the Cu K_α radiation.

Raman spectra were obtained with a Jobin-Yvon T64000 spectrometer equipped with a nitrogen-cooled CCD detector. The excitation was provided by an Ar–Kr ion laser and the spectra were recorded in a back-scattering configuration. The excitation line was at 514 nm and the excitation power was kept low enough to avoid heating of the samples.

3. Results and discussion

3.1. Elemental analysis results

The interaction between the laser beam and the target involves high energy processes, which can promote insertion of oxygen and/or nitrogen (the treatments were performed in air) in the layers formed on titanium targets. NRA analyses were performed to quantify the concentration of light elements at

the surface layers as a function of both the laser pulse duration and the laser fluence. Indeed, the intensity of NRA peaks is directly related to the concentration of the elements and to the cross-sections of the nuclear reactions considered [17–19].

For a given region of interest in a nuclear reaction spectrum, the number of recorded nuclear events is directly proportional to the number of nuclei to be analysed in the probed layer and to the number of incident ions. Concentration quantification is calibrated with a known standard whose composition has not to be close to the sample to be analysed. Assessment of the probe depth, both for the sample and the standard, is related to the stopping power (dE/dx) of the samples for the ions of the beam. In this megaelectronvolt energy range, stopping power data are known with accuracy better than 2% [20]. As the microbeam is composed of single charged $^2H^+$ ions, the count of the number of incident ions is achieved by measuring the number of positive charges which have reached the sample, usually equivalent to a few microCoulomb for a single spectrum. Since counting statistics are relatively high, mostly above a few thousands of events, the limiting step for the overall accuracy is charge measurement. Precision on concentration determination can then be estimated to about 5%.

The foreseen energies of the different nuclear reactions were checked on the spectra of standard samples, TiN and $CaCO_3$ (figures 2 and 3). Two nuclear reactions were used to quantify the concentration of nitrogen and oxygen.

Concerning nitrogen, the $^{14}N(d,\alpha_1)^{12}C$ nuclear reaction was used. It was induced by incident 1900 keV deuterons. It results in a peak in the 4500–5400 keV (figure 2) or 5500–6800 keV (figure 3(*b*)) energy range according to the thickness of the Mylar foil used (12 or 0 μm, respectively) which slows down the emitted alphas. The high stopping power for alpha particles produced in this reaction enables high depth resolution for a probed depth about 3 μm as shown in the inset of figure 2.

For oxygen, the $^{16}O(d,p_1)^{17}O$ nuclear reaction was used. The emitted proton group appears in the 1000–1300 keV (figure 2) or 700–900 keV (figure 3(*a*)) energy range, once again according to the Mylar foil used (12 or 23 μm, respectively) and to the incident deuteron energies (1900 and 920 keV, respectively). As seen from the spectrum of $CaCO_3$, a flat oxygen concentration depth profile leads to a plateau in the spectrum, thanks to a constant cross section of the $^{16}O(d,p_1)^{17}O$ reaction for incident deuterons between 920 and 790 keV. Thus, in any sample, the shape of the peak is a straight view of the in-depth oxygen profile.

The amount of carbon in the surface layers was estimated from the $^{12}C(d,p_0)^{13}C$ peak to be lower than 0.01 at%. This low amount of carbon can be explained by surface pollution of the samples, and thus the insertion of carbon in the target is negligible.

NRA spectra were treated off-line by means of the RISMIN code [21]. Results concerning oxygen and nitrogen concentrations calculated by using the PYROLE code are reported in table 3. It can be seen that nitrogen and oxygen are inserted in the target in different ways according to pulse duration.

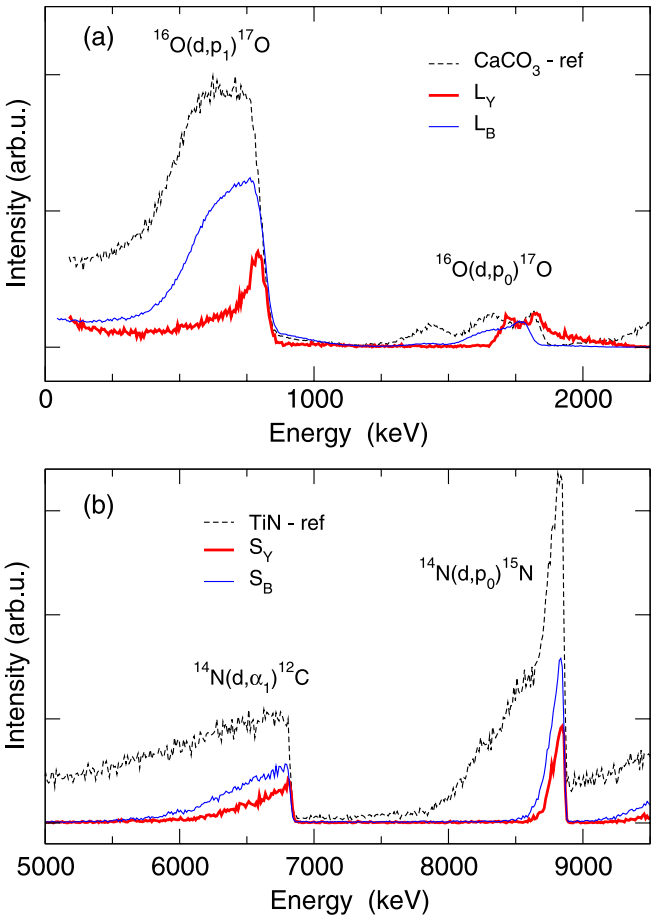

Figure 3. NRA spectra obtained with deuteron beams at 920 keV (*a*), and 1900 keV (*b*) for reference samples (dashed lines), yellow layers L_Y and S_Y (thick solid lines) and blue layers L_B and S_B (thin solid lines). A 23 μm thick Mylar foil was placed in front of the annular detector for the acquisition of spectrum (*a*). No Mylar foil was used in the case of spectrum (*b*).

In the case of long pulses (L_Y and L_B), the amount of oxygen is much higher than that of nitrogen. Indeed, the amount of nitrogen in sample L_B is smaller than 1 at%, which can be considered as the detection limit. By increasing the laser fluence (from L_Y to L_B), the oxygen amount increases from around 25 at% up to 64 at%, which corresponds to the growth of stoichiometric titanium dioxide (TiO_2), as previously reported [11]. Moreover, the composition of the layer L_B is constant within the probed depth up to 1 μm, but it is worth noting that the thickness of this layer is around 30 μm.

On the other hand, in the case of short pulses (S_Y and S_B), the amount of nitrogen is much higher than that of oxygen. The surface layer is composed mainly of titanium nitride including a small amount of oxygen (3–6 at%). By increasing the laser fluence, the amount of nitrogen increases mainly at the extreme surface of the layer. In addition, the increase in the number of pulses induces an increase in the oxygen amount in the layer [15].

3.2. *Structure and optical properties*

Figures 4 and 5 display, respectively, x-ray diffraction patterns and Raman spectra obtained for the samples described in

Table 3. Oxygen (right) and nitrogen (left) contents in atomic per cent of the four samples as determined from NRA analyses. Three zones were analysed, one close to the surface (0–0.25 μm), an intermediate one (0.25–0.50 μm) and a deeper one (0.50–0.75 μm).

Element		Oxygen (at%)				Nitrogen (at%)			
Samples		S_Y	L_Y	S_B	L_B	S_Y	L_Y	S_B	L_B
Probed depth (μm)	0–0.25	3	25	6	64	31	3	43	<1
	0.25–0.5	2	21	6	64	28	2	33	<1
	0.5–1.0	2	17	6	64	27	<1	23	<1

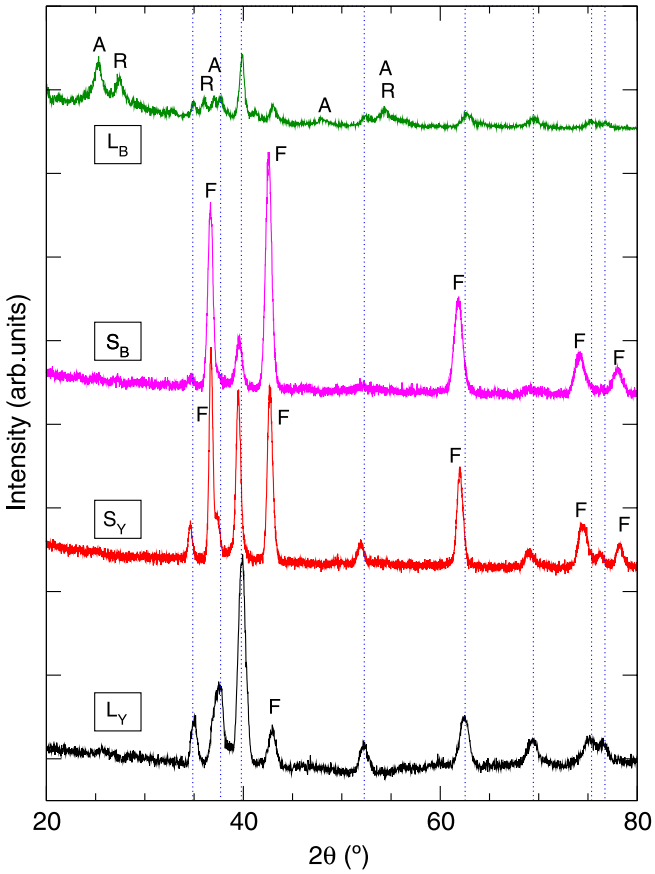

Figure 4. X-ray diffraction patterns of the four samples. From bottom to top: yellow layer obtained at 35 ns (L_Y), yellow layer obtained at 5 ns (S_Y), blue layer obtained at 5 ns (S_B) and blue layer obtained at 35 ns (L_B). Peaks labelled F correspond to face centered cubic phases. Vertical dotted lines indicate the Bragg reflections of hexagonal Ti_3O (JCPS-01-076-1644). For sample L_B (top), peaks corresponding to TiO_2 rutile (R) and anatase (A) phases are also indicated.

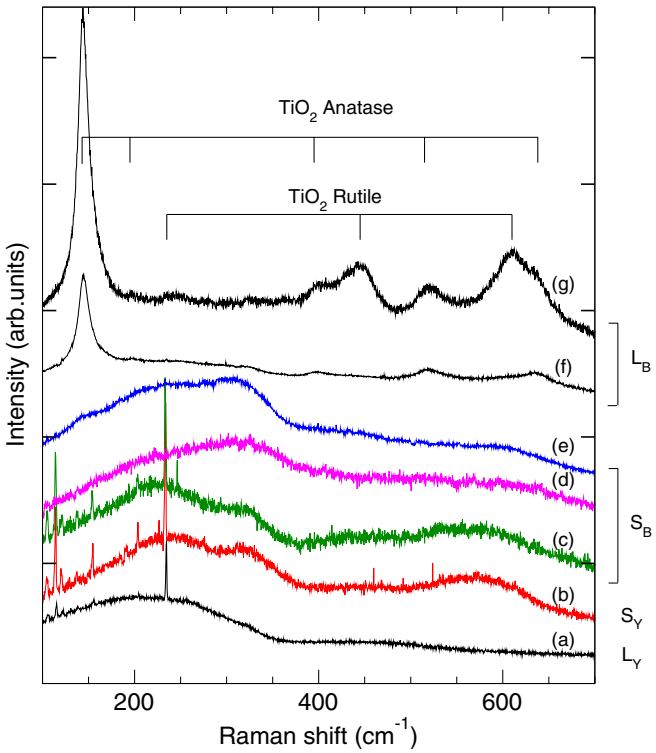

Figure 5. Raman spectra of the four samples. From bottom to top: yellow layers obtained at 35 ns (a) and 5 ns (b), and different zones of the blue layers obtained at 5 ns (c),(d),(e) and 35 ns (f),(g). Positions of characteristic TiO_2 rutile and anatase bands are indicated at the top. Spectra (a)–(d): sharp lines in the low frequencies range correspond to plasma lines of the Ar–Kr ion laser.

table 1. The first result to be noted is the quite different structures of layer L_B with respect to S_Y, S_B and L_Y layers. Peaks clearly associated with the anatase and the rutile phases of TiO_2 are observed both in the XRD pattern of layer L_B and in the related Raman spectrum [11, 22]. The presence of TiO_2 is in agreement with the results of elemental analysis of L_B layers. At the opposite, no peak can be assigned to TiO_2 in the XRD patterns of S_Y, S_B and L_Y layers. As previously observed, the diffraction peaks can be assigned to two families of phases [12]:

- A phase of hexagonal symmetry such as the Ti substrate, since the corresponding diffraction peaks fit to almost the same positions for all the samples. Quite similar to the Ti structure, insertion phases such as Ti_3O (JCPDS card 76-1644) and $TiN_{0.3}$ (JCPDS card 41-1352) could be in very good agreement with the experimental peak positions.
- A face centered cubic (fcc) phase. Contrary to the former ones the diffraction peaks are shifted slightly from one sample to another. Moreover, the relative intensity of these peaks, compared with those associated with the hexagonal phase, increases in the patterns of layers S_Y and S_B. Titanium nitride TiN (JCDPS 38-1420) and titanium monoxide TiO (JCPDS 08-0117) have fcc structures with close lattice parameters ($a_{TiN} = 4.242$ Å, $a_{TiO} = 4.177$ Å) which could be used to index the experimental peaks labelled F in figure 4. This matches with the formation of titanium oxynitrides shown by NRA analysis.

As mentioned above, bands associated with crystallized TiO_2 cannot be observed in the Raman spectra for S_Y, S_B and L_Y layers. Plasma laser lines (and Raman bands of the air)

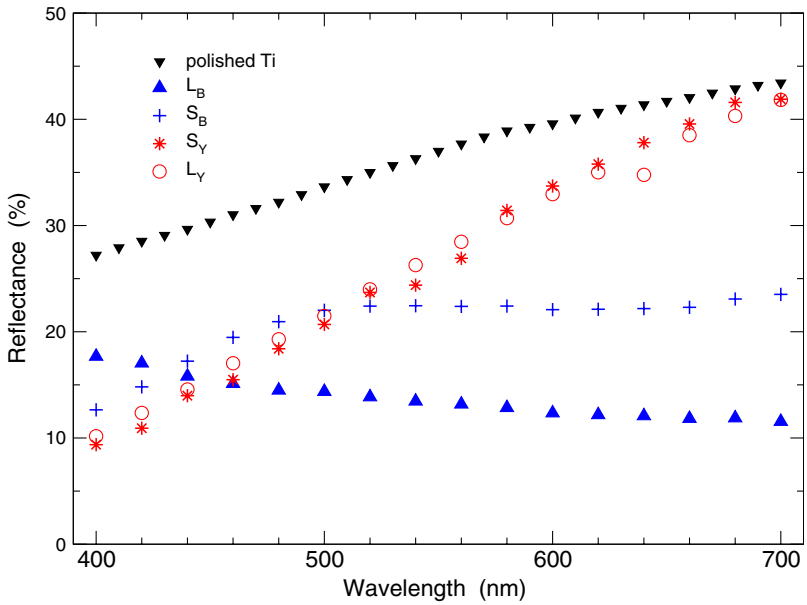

Figure 6. Reflectance spectra of the four samples. The spectrum corresponding to a polished titanium sample is presented for comparison.

are detected at low frequencies. Raman spectra display low intensity broad bands: a first band in the 100–350 cm^{-1} range and a second one of smaller intensity in the 500–600 cm^{-1} range. These spectra, mainly in the case of S_Y and S_B layers, are very similar to those reported for titanium nitrides [23] and oxynitrides [8, 24, 25]. Indeed, the fcc phases of TiN and TiO do not allow first order Raman modes. Thus, the experimental Raman spectra display only disorder-allowed modes and second-order scattering.

It is worth noting that significant changes were not found in the Raman spectra of the S_Y layer whatever the analysed point, while a significant broadening of the Raman bands was found for the layer S_B depending on the analysed zone (three spectra are shown in figure 5). A similar broadening of Raman bands had been reported in the case of PVD TiN layers doped with an increasing amount of oxygen, which gives rise to the amorphization of the layer and the appearance of poorly crystallized titanium dioxide [24]. Spectrum (e) in figure 5 exhibits around 142 cm^{-1} a shoulder suggesting the formation of amorphous titanium dioxide. NRA analysis of layer S_B showed a shallow depth increase in the concentration of nitrogen and twice as much oxygen amount than layer S_Y. This might lead to the growth of oxygen-enriched areas explaining the heterogeneity shown by Raman spectroscopy.

Concerning layer L_Y, a shift towards lower frequencies of the Raman bands is observed, mainly for the first band at about 220 cm^{-1}, with respect to those of layers S_Y and S_B. This difference in the Raman spectra can be correlated with the composition of the layer. L_Y contains almost 25 at% of oxygen but little nitrogen, whereas S_Y and S_B contain 30–40 at% of nitrogen and a small concentration of oxygen. Raman spectra of TiO is not well described in the literature, but a shift to lower frequencies with respect to the isostructural TiN bands is coherent with the higher atomic mass of oxygen.

Optical reflectance spectra of the four layers are presented in figure 6 together with the spectrum of the untreated substrate (polished titanium). The optical properties of the two yellow layers (S_Y and L_Y) do not differ significantly from the untreated substrate: they have a metal-like behaviour. This is supported by NRA results which indicate the growth of titanium nitride containing a low amount of oxygen in the case of S_Y layers, and the formation of understoichiometric titanium monoxide including a small amount of nitrogen in the case of L_Y layers. XRD patterns showed an fcc structure in both cases.

The two blue layers behave very differently from the yellow ones (S_B and L_B in figure 6). The observed optical reflectance of the blue L_B layer had been already reported by Perez del Pino *et al* for similar laser treatment conditions [25]. It is typical of the presence of titanium dioxide either in the form of rutile or anatase for which gap values around 3 eV correspond to the observed maximum of reflectance [26–28]. The second blue layer, S_B, obtained with the 5 ns source, exhibits a maximum shift towards visible range (500 nm) with a highest reflectance, close to the one of the yellow layers for $\lambda < 550$ nm. This optical behaviour, as well as Raman results, can be accounted for by the growth of heterogeneous layers containing titanium oxynitride together with oxygen-enriched areas close to titanium dioxide stoichiometry. Hence, the total reflectance of this layer S_B results from the weighted contributions of Ti(N,O) and titanium dioxide phases: spectrum S_B can be considered as a combination of spectra S_Y (or L_Y) and L_B. It should be noted that the amount of titanium dioxide in this S_B layer is small, as attested by a reflectance spectrum closer to the S_Y or L_Y ones than to the L_B one.

3.3. Thermal modelling of the laser–target interaction

The understanding of the phenomena occurring within the interaction zone between the laser beam and the target is a key point for explaining the influence of the laser treatment conditions on the structure and the properties of the formed

Table 4. Numerical simulation results obtained using the Semak model as a function of the laser treatment parameters: the laser pulse duration, τ and the laser irradiance, I. v_v indicates the evaporation front velocity, v_d the drilling velocity, v_m the lateral melt-ejection velocity, P_{abs} the power per unit length absorbed from the laser beam and P_{evap} that spent for evaporation.

Samples	S_Y	L_Y	S_B	L_B
τ (ns)	5	35	5	35
I (10^{12} W m^{-2})	8	1	15	2
v_v (m s^{-1})	95	10	215	30
v_d (m s^{-1})	90	10	200	30
v_m (m s^{-1})	600	250	800	380
P_{evap}/P_{abs}	1.0	0.7	1.0	0.9

surface layers. With the aim of estimating the relevance of the different phenomena in the laser–target interaction, numerical calculations were done using the physical model developed by Semak and Matsunawa [13].

The absorption of the laser beam at the target surface results in an increase in the surface temperature. The vaporization-induced recoil pressure increases with the surface temperature and gives rise to the ejection of molten metal at the edge of the interaction zone. The two phenomena, molten metal ejection and evaporation, provide the propagation of solid–liquid and liquid–vapour boundaries in the target analogously to drilling.

The Semak model analyses the energy balance in the laser–metal interaction zone taking into account the heat transfer due to recoil pressure induced-melt flow. Moreover, Semak showed that the fraction of the absorbed laser intensity carried away from the interaction zone due to evaporation increases when the absorbed laser intensity increases, while the fraction due to convection (lateral molten-ejection) decreases. It is worth noting that the Semak model describes drilling mechanisms in the continuous steady-state regime. A thermal simulation was carried out using the COMSOL MULTIPHYSICS code [29, 30], in which we take into account the beam energy absorption, the heat diffusion and the losses with the outside environment. This simulation shows that the surface reaches vaporization temperature very quickly and tends towards the limit indicated by Semak in his model.

Here, calculations performed in the case of 5 ns [12] and 35 ns pulse duration, with the laser irradiation conditions indicated in table 1, are compared in order to understand the observed differences in both structure and properties of the surface layers. Titanium physical properties were taken from [30]. Table 4 summarizes the most significant parameters calculated with this model: the evaporation front velocity, v_v, the drilling velocity, v_d, the melt-ejection velocity, v_m, and the fraction of the absorbed power which is spent in evaporation, P_{evap}/P_{abs}.

Results in table 4 show that the increase in the laser irradiance (i.e. the power density), I, induces the increase in the three velocities (v_v, v_m, v_m), as expected for a higher surface temperature, but the ratio of the melt-ejection to the evaporation velocities, v_m/v_{vap}, decreases from around 25 to 4. Thus, the propagation of the evaporation front accelerates with respect to that of the lateral melt-ejection front when the laser irradiance increases.

In the case of short pulses (S_Y and S_B), corresponding also to the highest irradiance values (8×10^{12} W m^{-2} and 15×10^{12} W m^{-2}, respectively), the calculated P_{evap}/P_{abs} ratio is equal to 1, which shows that almost all the absorbed energy is spent in evaporation. The liquid layer, formed at the beginning of the laser pulse, quickly disappears mainly by evaporation. Thus, every laser impact cleans off the target surface, and the final surface is determined only by the last laser impact. This result is consistent with previous estimation of the molten layer by Carpene *et al* [31]. The composition of layers S_Y and S_B shows that the insertion of nitrogen in the target dominates that of oxygen in the evaporation regime, but the increase in the laser fluence induces a higher insertion of oxygen, which is in agreement with the literature [32, 33].

In the case of longer pulses (L_Y and L_B), the calculated P_{evap}/P_{abs} ratio is lower than 1, which reveals a significant contribution of melt-ejection to the energy flux away from the interaction zone. The liquid layer increases during the laser pulse and it is laterally displaced under the action of the recoil pressure due to the matter evaporation. At the end of the laser pulse, one part of this liquid can return to the impact zone. The cumulative action of successive impacts gives rise to a rough surface. The insertion of oxygen is favoured in the liquid-ablation regime with respect to that of nitrogen. Moreover, the increase in the laser fluence leads to a higher insertion of oxygen, as it was also the case in the evaporation regime.

Finally, the increase in the laser fluence induces the increase in the P_{evap}/P_{abs} ratio in the liquid-ablation regime, which would lead to a transition to an evaporation regime.

4. Conclusion

Nitriding of titanium by pulsed laser irradiation in air is a reactive surface processing. The results obtained in this work underlined the strong influence of both laser pulse duration and fluence of near infrared Nd : YAG lasers on the nitriding efficiency and the properties of the formed surface layers. These two parameters determine the phenomena produced within the interaction zone between the laser beam and the target. The modelling of this interaction shows an evaporation regime in the case of short pulses, whereas a mixed liquid-ablation regime is found for the longer pulses.

Indeed, the evaporation regime achieved for the short pulse duration ($\tau = 5$ ns) favours the insertion of nitrogen in the target, giving rise to surface layers mainly composed of titanium nitride. The layers are thin and smooth as a consequence of the rapid disappearance of the liquid layer formed by the laser impact.

For the higher pulse duration, $\tau = 35$ ns, a mixed liquid-ablation regime is found. Almost no insertion of nitrogen occurs in the layers, which are mainly composed of titanium oxides. The insertion of oxygen increases with the fluence leading to a thick titanium dioxide layer displaying both anatase and rutile phases. In this case, both the thickness and the roughness of the layers increase with the laser fluence.

The colour of the layers is determined mainly by the laser fluence which favours the insertion of oxygen. In the case of low fluences, layers exhibit a yellow colour and metal-like

optical behaviour. Blue colour is obtained for high fluences with an optical behaviour going from mainly metal to insulator like as the pulse duration increases. This effect is related to the presence of a mixture of titanium oxynitride and titanium dioxide, the relative amounts of each other depending on the pulse duration.

Acknowledgments

The authors acknowledge CEA Valduc for providing one of the laser sources. This work has been financially supported by the Conseil Regional de Bourgogne.

References

[1] Sha W and Malinov S 2009 *Titanium Alloys: Modelling of Microstructure, Properties and Applications* (Cambridge: Woodhead Publishing)
[2] Zhecheva A, Sha W, Malinov S and Long A 2005 *Surf. Coat. Technol.* **200** 2192
[3] Laurens P, L'Enfant H, Sainte Catherine M C, Bléchet J J and Amouroux J 1997 *Thin Solid Films* **293** 220
[4] Raaif M, El-Hossary F M, Negm N Z, Khalil S M, Kolitsch A, Höche D, Kaspar J, Mändl S and Schaaf P 2008 *J. Phys. D: Appl. Phys.* **41** 085208
[5] Tian Y S, Chen C Z, Chen L X and Huo Q H 2005 *J. Phys. D: Appl. Phys.* **38** 4217
[6] Krishna D S R, Brama Y L and Sun Y 2007 *Tribol. Int.* **40** 329
[7] Dong H and Bell T 2000 *Wear* **238** 131
[8] Pérez del Pino A, Serra P and Morenza J L 2002 *Thin Solid Films* **415** 201
[9] Chappé J M, Vaz F, Cunha L, Moura C, Marco de Lucas M C, Imhoff L, Bourgeois S and Pierson J F 2008 *Surf. Coat. Technol.* **203** 804
[10] Lavisse L, Grevey D, Langlade C and Vannes B 2002 *Appl. Surf. Sci.* **186** 150
[11] Lavisse L, Jouvard J M, Imhoff L, Heintz O, Korntheuer J, Langlade C, Bourgeois S and Marco de Lucas M C 2007 *Appl. Surf. Sci.* **253** 8226
[12] Lavisse L, Sahour M C, Jouvard J M, Pillon G, Marco de Lucas M C, Bourgeois S and Grevey D 2009 *Appl. Surf. Sci.* **255** 5515
[13] Semak V and Matsunawa A 1997 *J. Phys. D: Appl. Phys.* **30** 2541
[14] Baüerle D 1996 *Laser Processing and Chemistry* (New York: Springer)
[15] Lavisse L, Jouvard J M, Gallien J P, Berger P, Grevey D and Naudy Ph 2007 *Appl. Surf. Sci.* **254** 916
[16] Berger P, Tominez E, Godart C, Alleno E, Daudin L and Gallien J P 2000 *J. Solid State Chem.* **154** 301
[17] Khodja H, Berthoumieux E, Daudin L and Gallien J P 2001 *Nucl. Instrum. Methods Phys. Res. B—Beam Interact. Mater. Atoms* **181** 83
[18] Cohen D D and Rose E K 1992 *Nucl. Instrum. Methods Phys. Res. B—Beam Interact. Mater. Atoms* **66** 158
[19] Gurbich A and Molodtsov S 2008 *Nucl. Instrum. Methods Phys. Res. B—Beam Interact. Mater. Atoms* **266** 1206
[20] Ziegler J F, Biersack J P and Littmark U 1985 *The Stopping and Range of Ions in Solids* (Pergamon: New York)
[21] Daudin L, Khojda H and Gallien J P 2003 *Nucl. Instrum. Methods Phys. Res. B—Beam Interact. Mater. Atoms* **210** 153
[22] Moret M P, Zallen R, Vijay D P and Desu S B 2000 *Thin Solid Films* **366** 8
[23] Spengler W, Kaiser R, Christensen A N and Müller-Vogt G 1978 *Phys. Rev.* B **17** 1095
[24] Trenczek-Zajac A, Radecka M, Zakrzewska K, Brudnik A, Kusior E, Bourgeois S, Marco de Lucas M C and Imhoff L 2009 *J. Power Sources* **194** 93
[25] Pérez del Pino A, Fernández-Pradas J M, Serra P and Morenza J L 2004 *Surf. Coat. Technol.* **187** 106
[26] Brudnik A, Bućko M, Radecka M, Trenczek-Zając A and Zakrzewska K 2008 *Vacuum* **82** 936
[27] Pascual J and Mathieu H 1978 *Phys. Rev.* B **18** 5606
[28] Tang H, Lévy F, Berger H and Schmid P E 1995 *Phys. Rev.* B **52** 7771
[29] COMSOL AB 2008 *COMSOL Multiphysics® 3.5a* (Stockholm, Sweden)
[30] Höche D, Shinn M, Kaspar J, Rapin G and Schaaf P 2007 *J. Phys. D: Appl. Phys.* **40** 818
[31] Carpene E, Schaaf P, Han M, Lieb K P and Shinn M 2002 *Appl. Surf. Sci.* **186** 195
[32] Höche D, Rapin G and Schaaf P 2007 *Appl. Surf. Sci.* **254** 888
[33] Schaaf P, Han M, Lieb K-P and Carpene E 2002 *Appl. Phys. Lett.* **80** 1091